Development of nanodrug-based eye drops with good penetration properties and ROS responsiveness for controllable release to treat fungal keratitis

Panhong Niu [1], Yuelan Wu[2,3], Fanxing Zeng[3], Shuping Zhang [1,3], Sijin Liu [3] and Hua Gao [2,3,4]

Abstract
Fungal keratitis is challenging to diagnose and treat and remains a significant cause of blindness worldwide. The easiest and most common method of drug delivery for patients with fungal keratitis is eye drop administration. However, the therapeutic effect of traditional eye drops is unsatisfactory, largely due to the intrinsic nature of the ocular barriers, which limit drug absorption; the rapid decrease in the drug concentration caused by tears; and the side effects induced by the uncontrolled release of ocular drugs. Oxidative stress and inflammation are the main causes of corneal tissue necrosis in fungal keratitis, and reducing reactive oxygen species (ROS) and the inflammatory response are important goals in developing drugs for fungal keratitis. In the current study, we developed a ROS-responsive and controllable nanocarrier (GC-EB) that efficiently delivered a clinically used antifungal drug, voriconazole (VOR), to treat fungal keratitis. In vitro and in vivo results demonstrated that the developed GC-EB-VOR exhibited high penetration through corneal barriers, good retention in the cornea and controllable drug release under low concentrations of ROS. As a result, ROS were effectively depleted and the inflammatory response was inhibited; thus, GC-EB-VOR shows promising antifungal efficacy. This work may provide a new strategy for developing nanodrugs to improve the therapeutic effect of eye drop instillation on fungal keratitis and reduce the risk of blindness.

Introduction

Fungal keratitis is a severe blinding ocular disease worldwide, accounting for approximately 39% of epidemic proportions in North India and 61.9% in North China[1-5]. *Fusarium* and *Aspergillus* are the most common pathogens, accounting for 37–62% and 24–30% of the total pathogens, respectively[6]. Common treatments for fungal keratitis include eye drops and lamellar and penetrating keratoplasty[7-9]. Compared with traumatic and expensive surgical treatments, eye drops are noninvasive, convenient, and generally accepted by patients with fungal keratitis[10].

However, the adsorption of traditional eye drops by topical ocular administration is limited due to the intrinsic nature of ocular barriers, which include the corneal double barriers that impede the penetration of water-soluble or lipid-soluble drugs, the blood-ocular barriers (blood-aqueous and blood−retinal), and tight junctions in the cornea[11-13]. Therefore, amphipathic eye drops are urgently needed. In addition, the corneal bioavailability for eye drops is commonly <5% because eye drops are substantially and rapidly cleared by tears within 30 s of administration[14], which greatly reduces the therapeutic efficacy of eye drops. Moreover, healthy corneal tissues inevitably suffer from the side effects of

Correspondence: Shuping Zhang (spzhang@sdfmu.edu.cn) or
Hua Gao (hgao@sdfmu.edu.cn)
[1]Biomedical Sciences College & Shandong Medicinal Biotechnology Centre, Shandong First Medical University & Shandong Academy of Medical Sciences, Jinan 250117, P. R. China
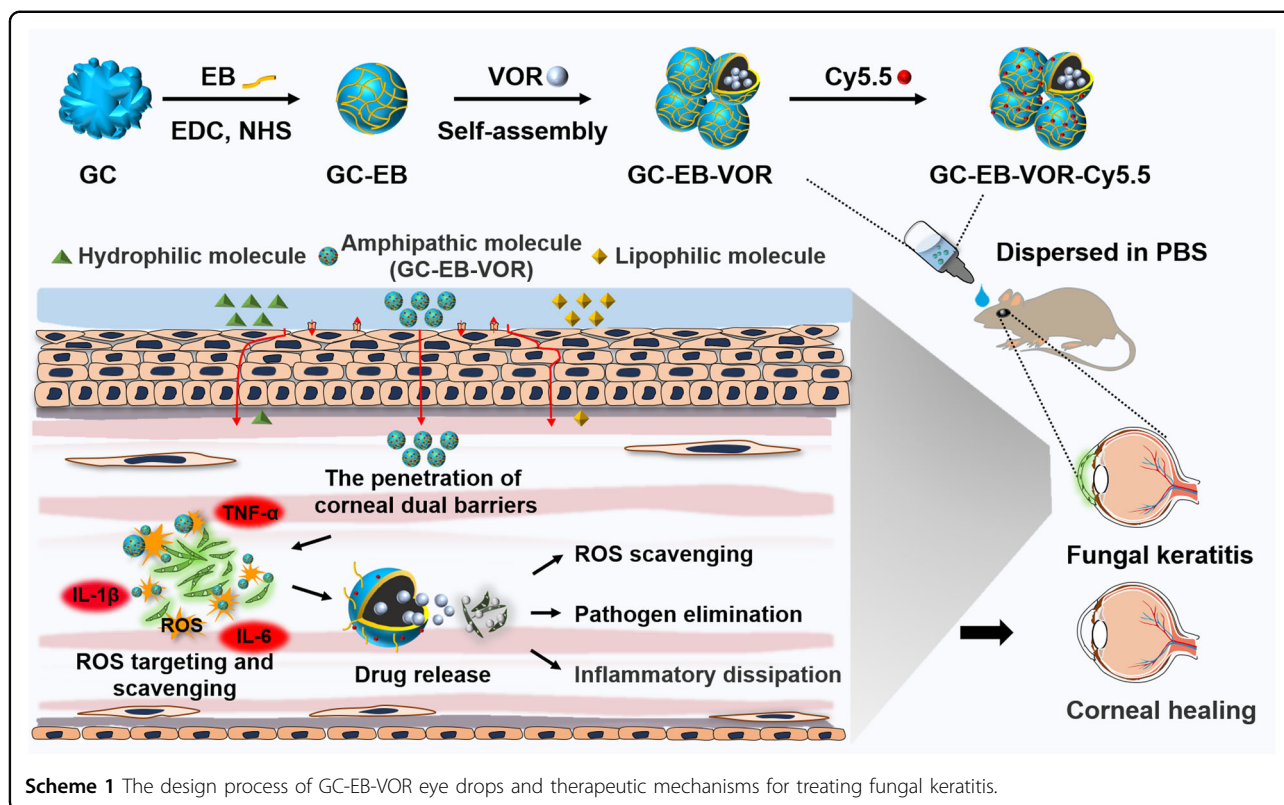[2]Medical College, Qingdao University, Qingdao, Shandong 266071, P. R. China
Full list of author information is available at the end of the article
These authors contributed equally: Panhong Niu, Yuelan Wu.

Scheme 1 The design process of GC-EB-VOR eye drops and therapeutic mechanisms for treating fungal keratitis.

uncontrolled release of ocular drugs. Thus, high penetration and controllable release of ocular drugs from eye drops could reduce the side effects and promote the retention of ocular drugs in a lesion[15]. However, there is still a lack of eye drop products that are responsive to this microenvironment and that can controllably release ocular drugs both spatially and temporally.

Glycol chitosan (GC), a derivative of chitosan (a widely used nanotherapeutic nanocarrier), exhibits high solubility and retains most of chitosan's properties, such as its antibacterial and amphiphilic properties. The acyl groups of GC were further used to functionalize and modify the hydrophobic functional groups to form an amphiphilic surface[16,17], which facilitated penetration through the multiple corneal barriers. Thus, GC could be a promising candidate for developing an amphipathic nanodrug to efficiently penetrate the hydrophilic and lipophilic corneal barriers. ROS-responsive biomaterials have been shown to alleviate oxidative stress and simultaneously deliver cargo in a controllable manner under certain scenarios, such as the inflammatory microenvironment in fungal keratitis[18,19]. The production of ROS in mouse corneas and human corneal epithelial cells (HCECs) was significantly increased upon exposure to fungi[20,21]. Furthermore, ROS were shown to damage the collagen matrix, resulting in corneal scarring, loss of corneal clarity, and impaired visual acuity[22,23]. Therefore, ROS-responsive release of
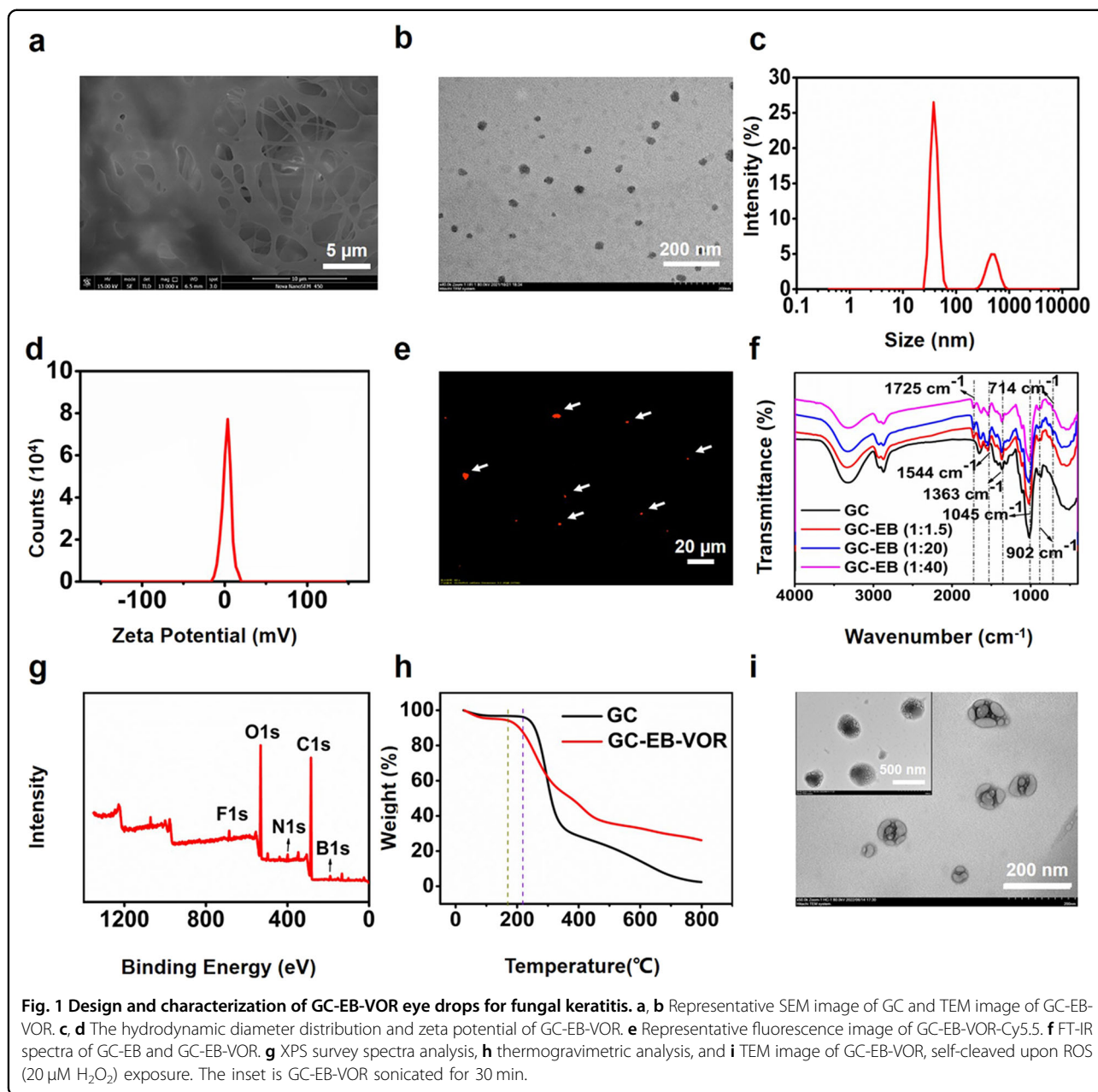
nanodrugs with simultaneous depletion of ROS is a promising strategy for fungal keratitis therapy.

In the present study, we used GC as a nanocarrier and 4-carboxyphenylboronic acid pinacol ester (EB) as a ROS-responsive group[15,24–26] to develop a ROS-controlled release polymeric nanocarrier (GC-EB) with effective penetration through ocular barriers (Scheme 1). GC-EB was loaded with a clinically used antifungal drug, voriconazole (VOR)[9,27,28], to treat fungal keratitis. Moreover, the surface of GC-EB-VOR was decorated with a Cy5.5 fluorescent molecule to track the nanodrug in vivo and in vitro. The developed GC-EB-VOR exhibited high penetration through the corneal barriers, controllable drug release under low concentrations of ROS, effective depletion of ROS, and promising antifungal efficacy, demonstrating potential for fungal keratitis therapy.

Results

Design and morphological characterization of GC-EB-VOR

To prepare the GC-EB-VOR nanodrug, EB was covalently bound to a GC polymer, followed by the incorporation of VOR. The self-assembly of GC-EB-VOR was initiated and driven by the amphiphilic nature of the polymer, in which the hydrophobic moieties faced the core and the hydrophilic moieties were exposed on the surface[17]. To track the biodistribution of GC-EB-VOR nanodrugs in vivo and vitro, GC-EB-VOR was labeled

Fig. 1 Design and characterization of GC-EB-VOR eye drops for fungal keratitis. a, **b** Representative SEM image of GC and TEM image of GC-EB-VOR. **c**, **d** The hydrodynamic diameter distribution and zeta potential of GC-EB-VOR. **e** Representative fluorescence image of GC-EB-VOR-Cy5.5. **f** FT-IR spectra of GC-EB and GC-EB-VOR. **g** XPS survey spectra analysis, **h** thermogravimetric analysis, and **i** TEM image of GC-EB-VOR, self-cleaved upon ROS (20 μM H_2O_2) exposure. The inset is GC-EB-VOR sonicated for 30 min.

with a Cy5.5 fluorescent molecule on the surface of the GC-EB-VOR nanodrug by an amidation reaction.

As revealed by a scanning electron microscopy (SEM) image of GC, multiple ultrathin and curved sheets were integrated into the porous architecture of GC (Fig. 1a). The macroporous skeleton of GC contained abundant cavities that were a few hundred microns in size. GC loaded with VOR spontaneously curled into a spherical morphology with the hydrophobic head inside and hydrophilic head outside in the two-phase solvent system[17,29−31]. The morphology characterization of GC-EB-VOR was revealed using transmission electron

microscopy (TEM) (Fig. 1b). Furthermore, GC-EB-VOR exhibited a predominant size of 38 nm, as revealed by dynamic light scattering analysis (Fig. 1c), consistent with the TEM results. A size >100 nm might be the result of agglomeration for some GC-EB-VOR particles. The zeta potential of GC-EB-VOR was 1.06 mV at pH 7.4 (Fig. 1d), facilitating the binding of the amino functional groups to the negatively charged cell membranes and thus penetration across the corneal barrier. The observation of red fluorescence demonstrated that the Cy5.5 molecule was successfully linked to the surface of GC-EB-VOR (Fig. 1e)[29,30,32].

Chemical bonding and stability assessment of GC-EB-VOR

Fourier transform infrared spectroscopy (FT-IR) spectra of GC and GC-EB are shown in Fig. 1f. The absorption bands at 1544 and 902 cm^{-1} were assigned to the vibration of C=C on the benzene ring. After introducing EB, bands at 1725, 714, 1045, and 1363 cm^{-1} were due to borate ester C=O stretching, B–O units, the vibration of the B–O–C bond and the anti-symmetric stretching vibration of B–O, respectively[33]. As demonstrated by X-ray photoelectron spectroscopy (XPS) analysis, the chemical bond peaks of GC-EB-VOR located at 210 eV, 284 eV, 397 eV, 530 eV and 710 eV resulted from B1s, C1s, N1s, O1s, and F1s[27,28], respectively (Fig. 1g). The high-resolution C1s spectra of GC-EB-VOR were deconvoluted into four subpeaks at 284.4, 285.1, 286.5, and 289.8 eV, which were attributed to C–C, C–OH, C–O–C and C=O groups, respectively (Fig. S1a). The O1s spectrum of GC-EB-VOR was deconvoluted into three individual peaks at 527.1 eV, 528.7 eV, and 530.4 eV (Fig. S1b). Two distinct peaks located at 707.4 eV and 721.5 eV were observed in the high-resolution B1s XPS spectra, which could be assigned to the B–C and B–O peaks, respectively, consistent with the FT-IR results. Taken together, these results indicated that borate ester modification was successfully introduced into GC to enable ROS responsiveness.

Thermogravimetric (TGA) analysis revealed that the weight of GC-EB-VOR decreased until the temperature increased to 200 °C (Fig. 1h), indicating the excellent stability of GC-EB-VOR under physiological conditions. GC-EB-VOR was also stable under long-term ultrasonic treatment. In contrast, GC-EB-VOR was easily degraded upon ROS stimulation, indicating that the nanodrug exhibited ROS-responsive self-cleavage (Fig. 1i).

Loading and release efficiency of VOR from GB-EB-VOR

The encapsulation and loading efficiency of drugs are two factors that directly affect the therapeutic efficacy of nanodrugs[34–36]. The concentrations of VOR ranged from 10 μg/mL to 3 mg/mL, resulting in VOR encapsulation rates up to 96% (Fig. 2a), and the loading efficiency of VOR in the GC-EB nanocarrier ranged from 7% to 77% (Fig. 2b). At pH 7.4 and 37 °C, GC-EB-VOR actively responded to ROS and efficiently released VOR upon treatment with H$_2$O$_2$ in a dose-dependent manner compared to the relatively slow VOR release in the PBS control group (Fig. 2c). An initial burst of VOR release, accounting for most of the total release of VOR, was observed at the first phase (<1 h) (Fig. 2c), probably due to the rapid diffusion of VOR from GC-EB-VOR. Given that the liquid solution in eye drops is limited and quickly removed, an initial burst release of VOR from GC-EB-VOR would be beneficial for treating fungal keratitis.

We next examined the ROS scavenging ability of GC-EB-VOR[37]. Compared to that of LPS-pretreated HCECs without GC-EB-VOR treatment, the level of ROS in lipopolysaccharide (LPS)-pretreated HCECs decreased after GC-EB-VOR treatment from 25 to 200 μg/mL in a dose-dependent manner[38,39] (Fig. 2d, e). This observation demonstrated the good antioxidant capacity of GC-EB-VOR[40]. From 25 to 200 μg/mL, the concentration of GC-EB-VOR did not exhibit cytotoxicity (Fig. 2f and S2), indicating that GC-EB-VOR exhibits good biocompatibility. In summary, these results revealed the satisfactory loading and release capacity of GC-EB for VOR with good biocompatibility and antioxidant capacity.

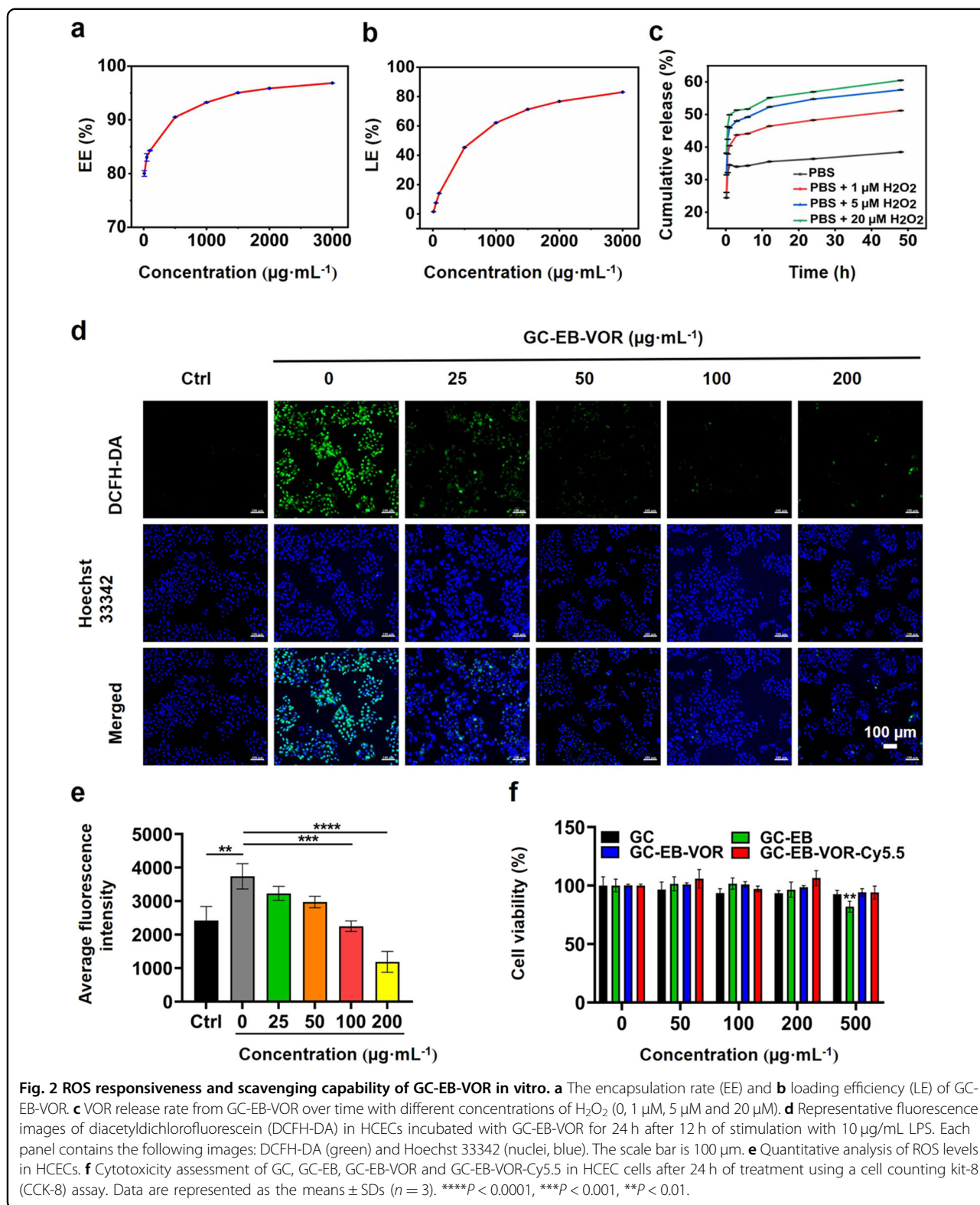### Cellular uptake and anti-inflammatory properties of GC-EB-VOR

Uptake and internalization by targeted cells are crucial for achieving therapeutic effects of nanodrugs. As shown in Fig. 3a, Cy5.5-derived red fluorescence was primarily localized in the cytoplasm, which indicated that the uptake of GC-EB-VOR by HCECs was excellent. The internalized nanodrugs were mainly transported and degraded through the endolysosomal pathways[41]. As expected, the red fluorescent signal of GC-EB-VOR was predominantly colocalized with the green fluorescent signal of Lyso-tracker, an indicator for late endosomes and lysosomes (Fig. 3b)[42].

After LPS stimulation, the production of cyclooxygenase-2 (*COX-2*), a key mediator of the inflammatory response, was induced in both HECEs (Fig. 3c) and RAW 264.7 cells (Fig. 3d)[43–45]. However, pretreatment with GC-EB-VOR inhibited LPS-stimulated *COX-2* production in a dose-dependent manner in HECEs and RAW 264.7 cells (Fig. 3c, d). The anti-inflammatory effect of GC-EB-VOR was validated by the decreased mRNA levels of proinflammatory cytokines in LPS-stimulated RAW 264.7 cells[46,47], including tumor necrosis factor α (TNF-α), interleukin 1β (IL-1β), and interleukin 6 (IL-6) (Fig. 3e).

Taken together, these results demonstrated that GC-EB-VOR was readily internalized and transported by the endolysosomal system in corneal epithelial cells. Furthermore, GC-EB-VOR exhibited a strong anti-inflammatory capacity.

Antifungal activity of GC-EB-VOR

Two representative fungal species, *Fusarium* and *Aspergillus flavus*, were cultured in LB medium and used to test the minimum inhibitory concentration (MIC) of GC-EB-VOR for fungi. The 90% inhibition of growth (MIC90) for *Fusarium* and *Aspergillus flavus* was 16 and 1 μg/mL, respectively (Fig. 4a and S3). Based on the loading and release efficiencies of VOR in GC-EB-VOR, 8 μg/mL and 0.5 μg/mL of VOR were the predicted

Fig. 2 ROS responsiveness and scavenging capability of GC-EB-VOR in vitro. a The encapsulation rate (EE) and **b** loading efficiency (LE) of GC-EB-VOR. **c** VOR release rate from GC-EB-VOR over time with different concentrations of H_2O_2 (0, 1 μM, 5 μM and 20 μM). **d** Representative fluorescence images of diacetyldichlorofluorescein (DCFH-DA) in HCECs incubated with GC-EB-VOR for 24 h after 12 h of stimulation with 10 μg/mL LPS. Each panel contains the following images: DCFH-DA (green) and Hoechst 33342 (nuclei, blue). The scale bar is 100 μm. **e** Quantitative analysis of ROS levels in HCECs. **f** Cytotoxicity assessment of GC, GC-EB, GC-EB-VOR and GC-EB-VOR-Cy5.5 in HCEC cells after 24 h of treatment using a cell counting kit-8 (CCK-8) assay. Data are represented as the means ± SDs ($n = 3$). ****$P < 0.0001$, ***$P < 0.001$, **$P < 0.01$.

MIC90 for *Fusarium* and *Aspergillus flavus*, respectively, and this was validated by treating fungi with pure VOR (Fig. 4b and S4). Thus, both GC-EB-VOR and pure VOR

significantly inhibited the growth of *Fusarium* and *Aspergillus flavus*. In contrast, GC and GC-EB did not exhibit obvious inhibitory activity against the growth of
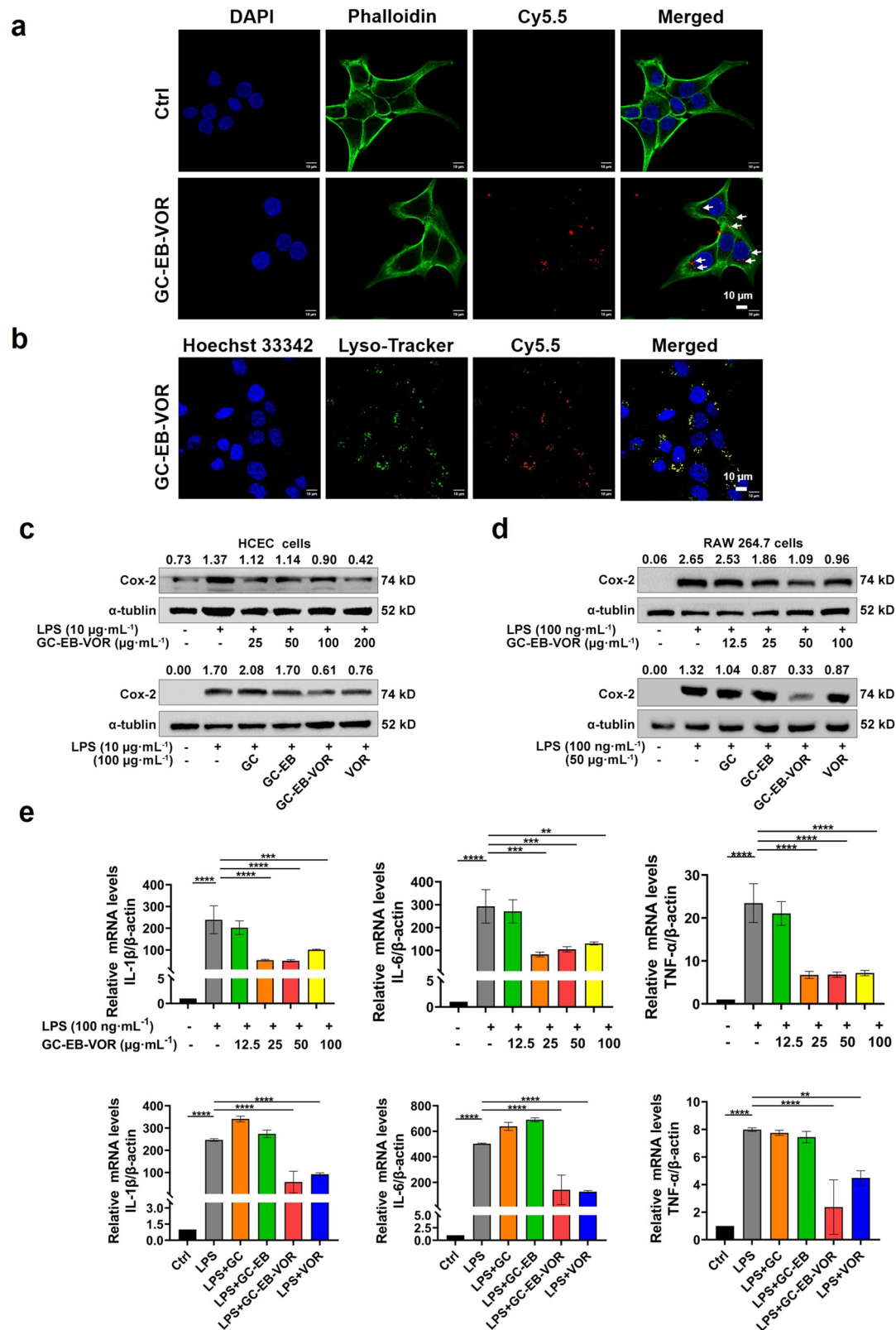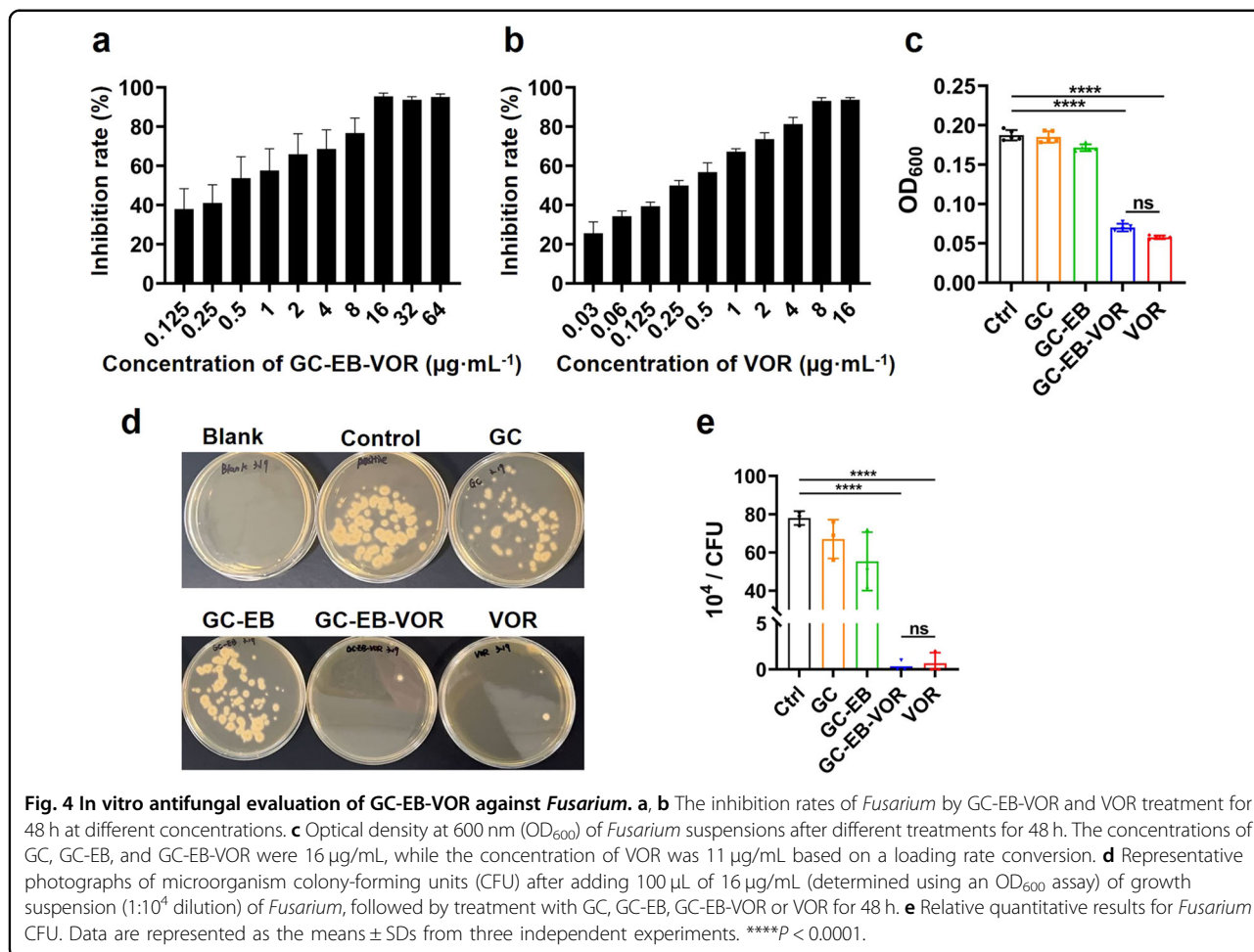
Fig. 3 (See legend on next page.)

Fig. 3 Localization and anti-inflammatory efficacy of GC-EB-VOR nanodrugs in HCEC cells. a Representative images showing the uptake of GC-EB-VOR by HCECs in vitro. The dyes phalloidin (green, 488 nm) and DAPI (blue, 408 nm) were used to visualize the cytoskeleton and nucleus, respectively. **b** Distribution of GC-EB-VOR-Cy5.5 (red, 561 nm) in intracellular lysosomes (green, 488 nm). **c** *Cox-2* levels in HCECs after 12 h of LPS preactivation and 24 h of various treatments. **d** *Cox-2* levels in RAW 264.7 cells after 6 h of LPS prestimulation and 6 h of different treatments. **e** Relative expression levels of the inflammatory factors IL-1β, TNF-α, and IL-6 in RAW 264.7 cells after treatment with GC, GC-EB, GC-EB-VOR, or VOR for 6 h. Scale bar = 10 μm. ($n = 3$). Data are represented as the means ± SDs from three independent experiments. ****$P < 0.0001$, ***$P < 0.001$, **$P < 0.01$.

Fig. 4 In vitro antifungal evaluation of GC-EB-VOR against *Fusarium*. a, **b** The inhibition rates of *Fusarium* by GC-EB-VOR and VOR treatment for 48 h at different concentrations. **c** Optical density at 600 nm (OD_{600}) of *Fusarium* suspensions after different treatments for 48 h. The concentrations of GC, GC-EB, and GC-EB-VOR were 16 μg/mL, while the concentration of VOR was 11 μg/mL based on a loading rate conversion. **d** Representative photographs of microorganism colony-forming units (CFU) after adding 100 μL of 16 μg/mL (determined using an OD_{600} assay) of growth suspension ($1:10^4$ dilution) of *Fusarium*, followed by treatment with GC, GC-EB, GC-EB-VOR or VOR for 48 h. **e** Relative quantitative results for *Fusarium* CFU. Data are represented as the means ± SDs from three independent experiments. ****$P < 0.0001$.

Fusarium and *Aspergillus flavus* (Fig. 4c–e and S5–7). These results demonstrated that GC-EB-VOR exhibited antifungal activity comparable to that of pure VOR, while GC-EB-VOR provided several additional benefits, such as ROS responsiveness and the ability to penetrate multiple ocular barriers.

Corneal injury attenuation after GC-EB-VOR treatment

To verify the antifungal capability of GC-EB-VOR in vivo, a fungal keratitis mouse model was established by injecting *Fusarium* spore solution to infect a wound on the cornea, according to an international general modeling method[9,21,48]. Then, mice were administered eye drops containing PBS, 1% GC, 1% GC-EB, 0.3% GC-EB-VOR, 1% GC-EB-VOR, or 1% VOR. As shown in Fig. 5a, slit-lamp examination indicated that compared to the control groups (PBS, 1% GC or 1% GC-EB), treatment with GC-EB-VOR and VOR (particular 1% GC-EB-VOR) inhibited fungal infection in the mouse corneas on Day 3 and particularly on Day 7. Histological examination verified that the corneal structure was recovered after GC-EB-VOR treatment. To quantify the therapeutic effect of GC-EB-VOR on fungal keratitis, we ranked fungal keratitis severity according to the area of corneal opacity, density of corneal opacity and surface regularity from Day 1 to Day 7[49]. Based on the score, fungal keratitis severity
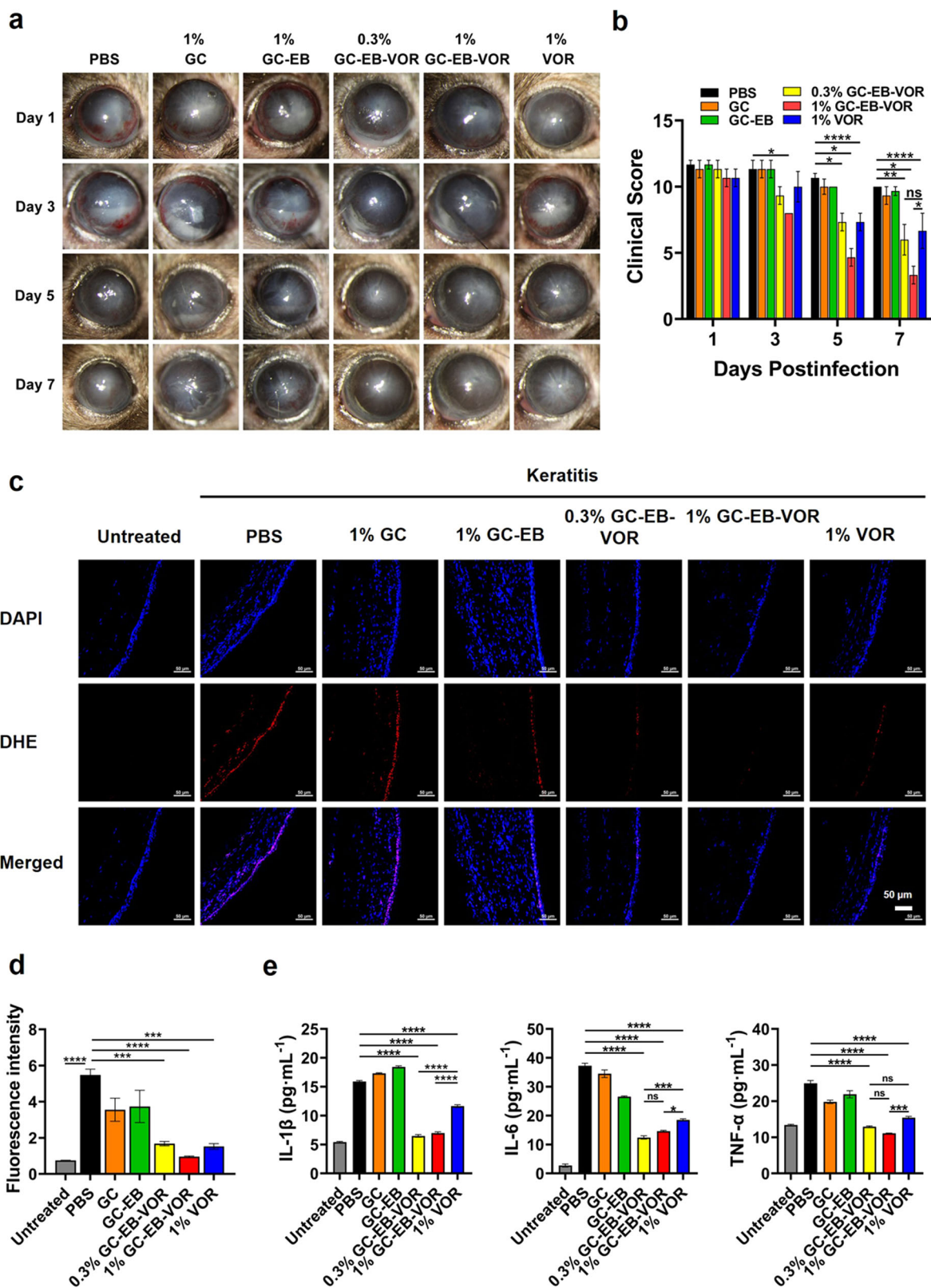
Fig. 5 (See legend on next page.)

(see figure on previous page)
Fig. 5 In vivo therapeutic efficacy of GC-EB-VOR eye drops in a mouse model with fungal keratitis. a Time course of the in vivo therapeutic efficacy of GC-based nanodrug and VOR eye drops after topical instillation in mice with fungal keratitis. Mice receiving PBS without nanomaterial served as a control (Ctrl) group. **b** Visual clinical scores. **c** Corneal tissue was stained with DHE (ROS content, red) and DAPI (nuclei, blue) to compare the ability of different treatments to respond to ROS. The scale bar is 50 μm. **d** Changes in corneal ROS levels in mice in each group. **e** ELISA was used to explore the expression of inflammatory factors (IL-1β, IL-6, and TNF-α) in corneal tissues treated with GC-based nanodrugs and free VOR. Data are represented as the means ± SDs from three independent experiments. ****$P < 0.0001$, ***$P < 0.001$, **$P < 0.01$, *$P < 0.05$.
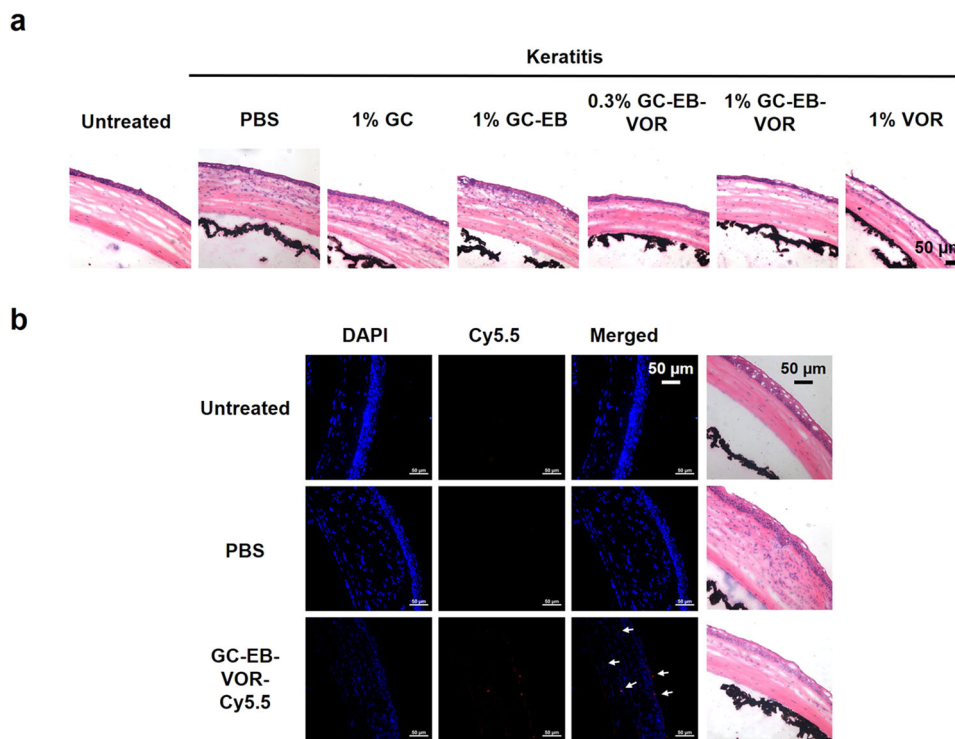

Fig. 6 Histology and in vivo localization analysis. a Histological examination of mouse cornea tissue sections with hematoxylin and eosin (H&E) staining for different treatment groups (scale bar = 50 μm). **b** Localization image of 1% GC-EB-VOR-Cy5.5 in mouse corneal tissue by fluorescence microscopy and histological examination of cornea tissue sections (H&E). Blue (DAPI) represents the nucleus, while red shows that the nanomaterial GC-EB-VOR was distributed in the full thickness of the cornea. Scale bar = 50 μm.

ranged from mild (≤5) to moderate (6–9) to severe (≥9) in mice. Consistent with the slit-lamp and histological examination observations, the fungal keratitis severity scores began to decrease in mice treated with 0.3% and 1% GC-EB-VOR and 1% VOR on Day 3 compared to the control groups (Fig. 5b). However, the scores for 1% GC-EB-VOR-treated mice were consistently lower than those of the other treatment from Days 3 to 7.

To substantiate the antioxidant and anti-inflammatory capabilities of GC-EB-VOR, we evaluated the levels of ROS and inflammatory factors in the corneal tissue of mice. ROS content measured via dihydroethidium (DHE) staining was reduced in mice treated with GC-EB-VOR and VOR compared to the control mice. (Fig. 5c, d). The infiltration of immune cells and the levels of inflammatory factors (IL-6, IL-1β, and TNF-α) were also reduced in mice treated with GC-EB-VOR compared to other mice (Fig. 5e).

Histological examination verified that the corneal structure was recovered after 7 days of treatment with GC-EB-VOR. Abnormal corneal architecture with high infiltration of immune cells was observed in the corneal stroma in the PBS, GC, and GC-EB groups but not in the GC-EB-VOR and VOR groups. Moreover, 1% GC-EB-VOR exhibited a better anti-inflammatory effect than that of 1% VOR (Fig. 6a). The visualization of Cy5.5 fluorescence after 7 days demonstrated that GC-EB-VOR was successfully delivered and accumulated in vivo (Fig. 6b).

Taken together, these results demonstrated the sustainable therapeutic effects of GC-EB-VOR on fungal keratitis in vivo, as revealed by the delivery and

accumulation of GC-EB-VOR in the cornea, reduced oxidative stress and inflammation, and attenuated corneal injury.

Discussion

The most common treatment for fungal keratitis is the administration of eye drops. The prerequisites for a promising outcome of antifungal eye drops include a wide antimicrobial spectrum, high sensitivity to fungus, and sufficient and sustained drug concentrations in the infected loci. VOR is a broad-spectrum antifungal drug widely included in eye drops with high sensitivity and low resistance to fungal infection[9,20,21]. Unfortunately, conventional eye drops have poor solubility and can be quickly removed after instillation in a short time; as a result, the concentration of drug retained in the lesion site is low and the antifungal efficacy is not exerted[14]. Moreover, the inherent corneal amphipathic barriers, the hydrophilic barrier of the corneal stroma, and the lipophilic barrier of the corneal epithelium[11−13] limit the penetration of commonly used fat-soluble drugs or water-soluble drugs and ultimately cause low corneal bioavailability of conventional eye drops. Thus, our first strategy was to adopt GC as a nanocarrier for VOR delivery to effectively penetrate the amphipathic barriers of the cornea.

As a natural cationic polymer polysaccharide, chitosan is widely used as a nanocarrier for nanotherapy[50−52] due to its exceptional properties, including superior biocompatibility, biodegradability, nontoxicity, low immunogenicity, low cost, and accessibility[53,54]. The quaternization of chitosan was found to enhance its hydrophilicity, antimicrobial activity and cellular uptake[55]. In addition, chitosan has been shown to maintain hemostasis and promote anti-inflammation and wound healing[56,57]. However, the application of chitosan is limited under physiological conditions due to its low solubility above pH 6.0[58]. GC is a derivative of chitosan with high solubility and retains several properties of chitosan, such as biodegradability, low immunogenicity, hemostasis, anti-inflammatory, and wound healing effects[53,54]. The amphiphilicity of GC polymers was shown to drive a self-assembly process in which hydrophobic groups oriented inward and the hydrophilic groups oriented outward[17], thus favoring the penetration of the hydrophilic and lipophilic corneal dual barriers. GC was previously used to penetrate miniature blood vessels and biofilm barriers in vivo[17,26,30]. More importantly, by ligating GC-EB-VOR with the Cy5.5 fluorescent molecule, our in vitro results revealed that GC-EB-VOR entered corneal cells to efficiently eliminate mycelia and accumulated in the lysosomes. Our in vivo results further demonstrated that GC-EB-VOR penetrated the corneal dual barriers and reached the corneal stroma, leading to a promising therapeutic effect on fungal keratitis.

Compared with other types of nano-ocular agents[10,59−62], such as contact lenses, eye drops and microspheres, our GC-EB-VOR exhibited several advantages, including a small size to facilitate penetration through the corneal barrier; in addition, GC-EB-VOR undergoes metabolic degradation in the lysosomes and is simple to prepare for mass production. Compared with traditional eye drops[11,14,63], GC-EB-VOR significantly increased the bioavailability of VOR through corneal penetration and thus reduced the frequency of eye drop instillations.

Stimuli-responsive self-assembled nanodrugs can release payloads at specific sites after endogenous or exogenous stimulation, such as pH, enzymatic, redox, thermal, magnetic, light, and ultrasonic stimuli[15,64−66]. Effective therapeutic outcomes and decreased side effects have been obtained by utilizing these types of nanodrugs in cancer therapy[15,67]. However, environment-responsive nanodrugs for ocular diseases have not been reported due to the delicate ocular barriers and relatively few blood vessels in ocular tissue. ROS are a well-known stimulus for the release of drugs from nanocarriers. For example, Ren et al. prepared a ROS-sensitive triblock copolymer, PEG-PUSe-PEG, to assemble nanoparticles that were oxidized and degraded under high concentrations of ROS, followed by a 100% release of the loaded Nile red molecules at 20 h[68]. Zheng et al. designed a ROS-responsive siRNA nanomedicine[26], 3I-NM@siRNA, that effectively released siRNA upon ROS stimulation and inhibited U87MG glioma xenotransplantation in situ in mice. Excess ROS are produced by the inflammatory response at the infection site of fungal keratitis[18,19]. Thus, we employed EB, a ROS-responsive group, to generate a tiny ball with a slowly releasing function for the sustained release of VOR in the infection loci. Surprisingly, the ROS scavenging ability of GC-EB-VOR was confirmed in vitro and in vivo, which indicated that the ROS-responsive controllable release of VOR was achieved, hopefully leading to a precise treatment for fungal keratitis.

Unexpectedly, we observed an inhibited inflammatory response in mice with fungal keratitis after treatment with our GC-EB-VOR drugs. The cornea is a type of transparent tissue. In fungal keratitis, excess ROS induces massive necrosis in the infection loci due to the infiltration of a large number of inflammatory cells, leading to cell proliferation and tissue repair. Consequently, scarring and the loss of corneal transparency occur even if the infection is controlled, resulting in vision loss or blindness[22,23]. GC-EB-VOR ultimately reduces the risk of blindness for patients with fungal keratitis by responding to ROS at the infection site while precisely releasing VOR to reduce inflammation and ROS.

Additionally, we observed an equal antifungal efficacy of GC-EB-VOR with VOR for *Fusarium* and *Aspergillus flavus*, the two most common fungi that cause fungal keratitis. Nonetheless, the instantaneous release rate of our GC-EB-VOR drug still needs to be improved to further increase the concentration of VOR at the lesion site and maximize its therapeutic effects on fungal keratitis.

Conclusions

In the current study, we designed and prepared a GC-EB-VOR nanodrug to treat fungal keratitis. In vitro and in vivo results revealed that GC-EB-VOR effectively penetrated the corneal dual barriers, produced ROS-responsive controllable release for antifungal activity, and remarkably attenuated corneal injury. Mechanistically, the successful delivery and accumulation of GC-EB-VOR in the cornea followed by the inhibition of oxidative stress and of the inflammatory response contributed to the therapeutic effect of GC-EB-VOR against fungal keratitis.

Materials and methods

Materials

GC, VOR, 4-carboxyphenylboronic acid pinacolate (EB), N-hydroxysuccinimide (NHS), and 1-(3-dimethylamino-propyl)-3-ethylcarbodiimide (EDC) were obtained from Sigma−Aldrich Co., Ltd. (Shanghai, China). N-hydroxysuccinimide was provided by TIC Co., Ltd. (Shanghai, China). Methanol and isopropanol were purchased from Sinopharm Chemical Reagent Co., Ltd. (Shanghai, China). Chromatographic grade acetonitrile was purchased from Yuwang Chemical Reagent Co., Ltd. (Shandong, China). HCECs (a human corneal epithelial cell line) and RAW 264.7 cells (a mouse mononuclear macrophage cell line) were obtained from the Cell Bank of the Chinese Academy of Science (Shanghai, China).

Synthesis of GC-EB-VOR

The synthesis diagram of GC-EB-VOR is presented in Scheme 1. Briefly, 0.816 g of EB was dissolved in 45 mL of methanol, and 15 mL of a 1.5 mg/mL GC aqueous solution was added and stirred well. Then, 0.563 g of NHS and 0.761 g of EDC were added and heated to 70 °C with stirring and reacted for 24 h. After 3 days of dialysis, EB-modified GC-EB was obtained by freeze-drying. Then, 0.01 g of GC-EB was prepared in 15 mL of distilled water with sonication treatment for 15 min. Next, 0.04 g of VOR in 2 mL of isopropanol-ethanol was added into the GC-EB solution system, replenished with 3 mL isopropanol-ethanol solution, and stirred for 24 h. The GC-EB-VOR ROS-responsive nanodrug was obtained by freeze-drying after dialysis.

Characterization of the nanodrugs

The microstructure of the as-prepared materials was characterized using a scanning electron microscope (NOVA Nano SEM 450, FEI, USA) and a transmission electron microscope (HT7800, HITACHI, Japan). The FT-IR spectra were collected using a Fourier transform infrared spectrometer (Nicolet iS5, ThermoScientific, USA). The surface chemical compositions of sorbents were characterized using X-ray photoelectron spectroscopy (XPS, Escalab 250Xi, ThermoScientific, USA) with 1486.6 eV radiation as the excitation source. The TGA curves were determined using a thermal gravimetric analyzer (TG209 F3, Netzsch, Germany) and ranged from room temperature to 900 °C at a heating rate of 10 K/min under a N_2 atmosphere. The zeta potential of the nanodrugs was determined using a Zetasizer Nano series ZS instrument (Zetasizer Nano ZS90, Malvern, UK). Confocal laser scanning microscopy images of cells were obtained using an Olympus confocal microscope system (FV12-IXCOV, Olympus, Japan). The fluorescence was quantitatively measured using an inverted fluorescence microscope (Axio vert A1, Zeiss, Germany). The gel electrophoresis images were obtained using a Molecular Imager FX (ChemiDoc XRS+, Bio-Rad, USA).

High-performance liquid chromatography (HPLC) analysis

The content of VOR in GC-EB-VOR was analyzed by using a Waters ACQUITY UPLC® H-Class system with a UV−vis detector. VOR was separated by a C18 column (Hypersil ODS2, 150 mm length × 4.6 mm i.d., 5 μm). A mixture of 70% HPLC-grade methanol and 30% Millipore water was used as the mobile phase. The flow rate was 0.6 mL/min. The detection wavelength was 260 nm, and the injection volume was 10 μL. To investigate the encapsulation efficiency (EE) and loading efficiency (LE) of drugs, the following steps were performed: VOR solutions at different concentrations (m_0; 10, 50, 100, 500, 1000, 1500, 2000, and 3000 μg/mL) were added to 500 μg/mL GC-EB solution (m) and stirred for 24 h. Then, the supernatant of the solution was filtered through a filter membrane to detect the unreacted concentration (m_1) of VOR by the HPLC system. The drug encapsulation content and loading amount were calculated according to related formulas as follows:

$$EE\% = \frac{m_0 - m_1}{m_0} \times 100\%$$

$$LE\% = \frac{m_0 - m_1}{m} \times 100\%$$

The release profiles of VOR from GC-EB-VOR were used to investigate the ROS responsiveness property. GC-EB-VOR was incubated with 0, 1, 5, or 20 μM H_2O_2 for varying periods of time (0.5 h–50 h) in dialysis bags. PBS was used as a control under the same conditions. Afterward, the dialyzed solutions were quantified by HPLC.

Cytotoxicity assay

HCECs were cultured at 37 °C under 5% CO_2 with Dulbecco's modified Eagle medium (DMEM)-F12 supplemented with 10% fetal bovine serum and 1% penicillin−streptomycin. RAW 264.7 cell lines were cultured in DMEM, with supplementation and culture conditions consistent with the HCEC cells. Cell viability was measured via a CCK-8 assay. In brief, 1×10^4 cells/well were seeded in 96-well microplates and cultured for 24 h. Cells were subsequently treated with drugs and cultured for 24 h. Then, cells were incubated with the CCK-8 solution for 4 h. The optical density (both the experimental and blank groups) of the incubated cells was determined using a multifunctional microplate reader at 450 nm.

Detection of ROS

HCECs were seeded in a six-well cell culture plate at a density of 1×10^5 cells/mL and cultured for 24 h. The cells were then stimulated with LPS (1 µg/mL) to observe an inflammatory state and treated with different concentrations of GC-EB-VOR (0, 25, 50, 100, or 200 µg/mL) for 24 h. Subsequently, the cells were incubated with diacetyldichlorofluorescein (DCFH-DA; 5 µM, Beyotime Biotechnology, China) for 20 min at 37 °C. The cells were washed three times with serum-free cell culture medium to sufficiently remove DCFH-DA that did not enter the cells. The fluorescence signals were detected with a fluorescence microscope. The fluorescence intensity was analyzed by the analytical method included with the microscope. The experiment was conducted three times.

Cellular uptake and localization

Briefly, 1×10^5 HCEC cells/well were plated in a confocal dish, incubated for 24 h, and then stimulated with LPS for 12 h. Then, 100 µg/mL GC-EB-VOR-Cy5.5 was added, and the cells were incubated in the dark for 24 h to release the drug completely. The cells were fixed with 4% paraformaldehyde. FITC-phalloidin was used for staining, and the cells were incubated in the dark for 30 min at room temperature. The nuclei were stained with DAPI and observed under a confocal microscope. For intracellular localization experiments, HCECs were cultured with GC-EB-VOR-Cy5.5 for 24 h and then stained and analyzed by confocal microscopy. Lysosomes were stained with LysoTracker Green (50 nM, 30 min), and the nuclei were stained with Hoechst 33342 (200 nM, 20 min).

Western blot analysis

Cells were lysed in a 100:1:1 mixture of RIPA buffer:-protein phosphatase inhibitor-PMSF, and the protein concentration was determined with a Pierce BCA protein assay kit. Electrophoresis was performed using sodium dodecyl sulfate−polyacrylamide gel electrophoresis (SDS−PAGE), and protein was transferred to polyvinylidene fluoride (PVDF) membranes. The membranes were shaken in 5% skim milk (dissolved in Tris-buffered saline with 0.1% Tween 20; TBST) on a shaker for 1 h at room temperature. After being washed with TBST three times, primary antibodies diluted 1:1000 in TBST were incubated overnight at 4 °C. This was followed by incubation with a secondary antibody (1:5000) for 1 h at room temperature. Densitometry analysis was performed using Bio-Rad Image Lab computer software after the samples were washed three times with TBST.

Real-time RT−PCR

RNA extraction, reverse transcription and cDNA PCR amplification were completed by conventional methods[69]. The primer sequences used in the research were as follows: 5'-GATTACTGCTCTGGCTCCTAGC-3' (*β-actin* forward), and 5'-GACTCATCGTACTCCTGCTTGC-3' (*β-actin* reverse); 5'-CGCAGCAGCACATCAACAAGAGC-3' (*IL-1β* forward), and 5'-TGTCCTCATCCTGGAAGGTCCACG-3' (*IL-1β* reverse); 5'-CACAAGTCCGGAGAGGAGAC-3' (*IL-6* forward), and CAGAATTGCCATTGCACAAC-3' (*IL-6* reverse); 5'-ACCCTCACACTCAGATCATCTT-3' (*TNF-α* forward), and 5'-GGTTGTCTTTGAGATCCATGC-3' (*TNF-α* reverse).

Antifungal activity studies

Standard *Fusarium* and *Aspergillus fumigatus* strains were provided by the Shandong Institute of Ophthalmology. The MIC test was based on the CLSI M38-A2[70] broth microdilution method. Briefly, fungal conidia were obtained from Sabouraud medium, and the density of the conidial suspension was adjusted spectrophotometrically at 530 nm (0.15–0.17 for *Fusarium*, 0.09–0.13 for *Aspergillus fumigatus*) and diluted 1:50 in RPMI-1640 medium. In 96-well polystyrene cell culture trays, different concentrations of drugs and conidia suspensions were added at a ratio of 1:1, incubated for 46–50 h in an aerobic incubator without CO_2 at 35 °C, and then absorbances were read at 600 nm with a microplate reader. MIC90 was defined as the minimum drug concentration that inhibited 90% of the growth of the fungus. The fungal suspension was then treated with or without GC-EB-VOR at a concentration of 16 µg/mL, and the PBS-treated group served as a control. The absorbance at 600 nm (OD_{600}) was detected by a microplate reader, and the number of fungal colonies was visually compared by the colony-forming unit (CFU) method.

Establishment of the fungal keratitis model

Female C57BL/6 J mice (6–8 weeks old) were purchased from Beijing Vital River Laboratory Animal Technology Co., Ltd. The mice were treated in accordance with the

guidelines provided by the Association for Research in Vision and Ophthalmology. The study protocols were approved by the Ethics Committee of Shandong First Medical University (Shandong Academy of Medical Sciences). The mice were anesthetized by intraperitoneal injection of 0.06% sodium pentobarbital, a 2 mm area of the central corneal epithelium of the right eye was removed, and the cornea was cross-scratched. Then, 5 μL of *Fusarium* solution (1×10^8 CFU/mL) was dripped on the cornea and covered with a soft contact lens. Subsequently, the eyelids were sutured. One day after infection, stitches were removed, and nanomedicine drops (10 μg/mL) were administered topically four times per day for seven consecutive days. Photographs of the mouse eyes at Days 1, 3, 5, and 7 were obtained with a slit-lamp microscope and scored to analyze inflammation development as previously published[49]. After the mice were humanely euthanized, the eyeballs were removed for histological analysis, immunohistochemical staining, and ELISA detection.

Histopathological examination

On the seventh day after infection, the eyeballs of mice were harvested, fixed, frozen, and stained with hematoxylin and eosin. The structure was observed using a fluorescence microscope to determine the histopathological changes in the cornea.

Immunofluorescence

A ROS fluorescent probe DHE kit (Wuhan Servicebio Biotechnology Co., Ltd.) was used to determine the ROS activity of the corneas of mice with fungal keratitis after drug treatment. Fresh corneal tissue was embedded in optimum cutting temperature compound to prepare frozen sections with a thickness of 10 μm. Precooled phosphate-buffered normal saline at 4 °C was used to cover the corneal tissue, and the corneal tissue was removed from the saline after gentle shaking. A working solution containing 5 μM DHE was added and incubated for 20 min in a 37 °C incubator. The working solution was removed, and the slides were sealed after rinsing with the cleaning solution and then observed under a fluorescence microscope and photographed.

Enzyme-linked immunosorbent assay (ELISA)

Mouse corneas ($n = 6$/group) were collected and centrifuged to obtain supernatant. ELISA kits (ABclonal Biology) were used to quantify IL-6, IL-1β, and TNF-α protein levels. Each well was charged with 100 μL of the sample solution, and the absorbance was determined at 450 nm using a reference wavelength of 630 nm.

Statistical analysis

The difference between the two groups was evaluated using Student's *t* test. One-way analysis of variance was used to analyze differences between three or more groups. When $P < 0.05$, the difference was considered significant. To ensure the repeatability of all experiments, each experiment was repeated three times, and the representative experimental data were expressed as the mean standard deviation (SD).

Author details
¹Biomedical Sciences College & Shandong Medicinal Biotechnology Centre, Shandong First Medical University & Shandong Academy of Medical Sciences, Jinan 250117, P. R. China. ²Medical College, Qingdao University, Qingdao, Shandong 266071, P. R. China. ³Medical Science and Technology Innovation Center, Shandong First Medical University & Shandong Academy of Medical Sciences, Jinan, Shandong 250117, P. R. China. ⁴State Key Laboratory Cultivation Base, Shandong Provincial Key Laboratory of Ophthalmology, Eye Institute of Shandong First Medical University, Qingdao, China

Author contributions
P.N., S.Z., and H.G. designed the project. N.P., W.Y., Z.F., and Y.B. performed the experiments and analyzed the results. S.L. and H.G. provided useful suggestions for this project. P.N., W.Y., and S.Z. wrote and revised the manuscript.

Data availability
The data that support the plots within this paper and other findings of this study are available from the corresponding authors upon reasonable request.

Conflict of interest
The authors declare no competing interests.

Publisher's note
Springer Nature remains neutral with regard to jurisdictional claims in published maps and institutional affiliations.

Supplementary information The online version contains supplementary material available at https://doi.org/10.1038/s41427-023-00478-9.

References
1. Chowdhary, A. & Singh, K. Spectrum of fungal keratitis in North India. *Cornea.* **24**, 8–15 (2005).
2. Xie, L., Zhong, W., Shi, W. & Sun, S. Spectrum of fungal Keratitis in North China. *Ophthalmology.* **113**, 1943–1948 (2006).
3. Chang, D. C. et al. Multistate outbreak of Fusarium keratitis associated with use of a contact lens solution. *JAMA* **296**, 953–963 (2006).
4. Ahn, M., Yoon, K. C., Ryu, S. K., Cho, N. C. & You, I. C. Clinical aspects and prognosis of mixed microbial (bacterial and fungal) keratitis. *Cornea.* **30**, 409–413 (2011).
5. Brown, L., Leck, A. K., Gichangi, M., Burton, M. J. & Denning, D. W. The global incidence and diagnosis of fungal keratitis. *Lancet Infect. Dis.* **21**, e49–e57 (2021).
6. Sharma, N. et al. Fungal keratitis: a review of clinical presentations, treatment strategies and outcomes. *Ocul. Surf.* **24**, 22–30 (2022).

7. Tanure, M. A., Cohen, E. J., Sudesh, S., Rapuano, C. J. & Laibson, P. R. Spectrum of fungal keratitis at Wills Eye Hospital, Philadelphia, Pennsylvania. *Cornea.* **19**, 302–312 (2000).

8. Panda, A., Sharma, N., Das, G., Kumar, N. & Satpathy, G. Mycotic keratitis in children: epidemiologic and microbiologic evaluation. *Cornea.* **16**, 295–299 (1997).

9. Huang, J. F. et al. A hydrogel-based hybrid theranostic contact lens for fungal Keratitis. *ACS Nano* **10**, 6464–6473 (2016).

10. Li, L. et al. Antioxidant and anti-glycated TAT-modified platinum nanoclusters as eye drops for non-invasive and painless relief of diabetic cataract in rats. *Chem. Eng. J.* **398**, 125436 (2020).

11. Huang, D., Chen, Y. S. & Rupenthal, I. D. Overcoming ocular drug delivery barriers through the use of physical forces. *Adv. Drug. Deliv. Rev.* **126**, 96–112 (2018).

12. Josyula, A. et al. An ion-paired moxifloxacin nanosuspension eye drop provides improved prevention and treatment of ocular infection. *Bioeng. Transl. Med.* **6**, e10238 (2021).

13. Freddo, T. F. A contemporary concept of the blood-aqueous barrier. *Prog. Retin. Eye Res.* **32**, 181–195 (2013).

14. Lanier, O. L. et al. Review of approaches for increasing ophthalmic bioavailability for eye drop formulations. *AAPS PharmSciTech* **22**, 107 (2021).

15. Li, D., Zhang, R., Liu, G., Kang, Y. & Wu, J. Redox-responsive self-assembled nanoparticles for cancer therapy. *Adv. Healthc. Mater.* **9**, e2000605 (2020).

16. Kim, C. S. et al. Glycol chitosan-based tacrolimus-loaded nanomicelle therapy ameliorates lupus nephritis. *J. Nanobiotechnol.* **19**, 109 (2021).

17. Ryu, J. H., Yoon, H. Y., Sun, I. C., Kwon, I. C. & Kim, K. Tumor-targeting glycol chitosan nanoparticles for cancer heterogeneity. *Adv. Mater.* **32**, e2002197 (2020).

18. Yao, Y. et al. Reactive oxygen species (ROS)-responsive biomaterials mediate tissue microenvironments and tissue regeneration. *J. Mater. Chem. B* **7**, 5019–5037 (2019).

19. Mittal, M., Siddiqui, M. R., Tran, K., Reddy, S. P. & Malik, A. B. Reactive oxygen species in inflammation and tissue injury. *Antioxid. Redox Signal.* **20**, 1126–1167 (2014).

20. Hua, X. et al. ROS-induced oxidative injury involved in pathogenesis of fungal keratitis via p38 MAPK activation. *Sci. Rep.* **7**, 10421 (2017).

21. Leal, S. M. Jr. & Pearlman, E. The role of cytokines and pathogen recognition molecules in fungal keratitis-insights from human disease and animal models. *Cytokine.* **58**, 107–111 (2012).

22. Hazlett, L., Suvas, S., McClellan, S. & Ekanayaka, S. Challenges of corneal infections. *Expert Rev. Ophthalmol.* **11**, 285–297 (2016).

23. Ibrahim Al-Mashahedah, A. M., Kanwar, R. K. & Kanwar, J. R. Utility of nanomedicine targeting scar-forming myofibroblasts to attenuate corneal scarring and haze. *Nanomedicine.* **14**, 1049–1072 (2019).

24. Su, Z. et al. ROS-triggered and regenerating anticancer nanosystem an effective strategy to subdue tumor's multidrug resistance. *J. Control Release* **196**, 370–383 (2014).

25. Tapeinos, C. & Pandit, A. Physical, chemical, and biological structures based on ROS-sensitive moieties that are able to respond to oxidative microenvironments. *Adv. Mater.* **28**, 5553–5585 (2016).

26. Zheng, M. et al. ROS-responsive polymeric siRNA nanomedicine stabilized by triple interactions for the robust glioblastoma combinational RNAi therapy. *Adv. Mater.* **31**, e1903277 (2019).

27. Khan, N. A., An, H. J., Yoo, D. K. & Jhung, S. H. Polyaniline-derived porous carbons: Remarkable adsorbent for removal of various hazardous organics from both aqueous and non-aqueous media. *J. Hazard Mater.* **360**, 163–171 (2018).

28. Stuart et al. Effect of combinations of additives on the performance of lithium ion batteries. *J. Power Sources* **194**, 1053–1060 (2009).

29. Kim, K. et al. Physicochemical characterizations of self-assembled nanoparticles of glycol chitosan-deoxycholic acid conjugates. *Biomacromolecules.* **6**, 1154–1158 (2005).

30. Kim, K. et al. Tumor-homing multifunctional nanoparticles for cancer theragnosis: Simultaneous diagnosis, drug delivery, and therapeutic monitoring. *J. Control Release* **146**, 219–227 (2010).

31. Saravanakumar, G. et al. Hydrotropic oligomer-conjugated glycol chitosan as a carrier of paclitaxel: synthesis, characterization, and in vivo biodistribution. *J. Control Release* **140**, 210–217 (2009).

32. Nair, M., Johal, R. K., Hamaia, S. W., Best, S. M. & Cameron, R. E. Tunable bioactivity and mechanics of collagen-based tissue engineering constructs: A

comparison of EDC-NHS, genipin and TG_2 crosslinkers. *Biomaterials.* **254**, 120109 (2020).

33. Agathopoulos, S. et al. Formation of hydroxyapatite onto glasses of the CaO-MgO-SiO$_2$ system with B$_2$O$_3$, Na$_2$O, CaF$_2$ and P$_2$O$_5$ additives. *Biomaterials* **27**, 1832–1840 (2006).

34. Yeo, Y. & Park, K. Control of encapsulation efficiency and initial burst in polymeric microparticle systems. *Arch. Pharm. Res.* **27**, 1–12 (2004).

35. Cai, K. et al. Dimeric drug polymeric nanoparticles with exceptionally high drug loading and quantitative loading efficiency. *J. Am. Chem. Soc.* **137**, 3458–3461 (2015).

36. Achouri, D., Alhanout, K., Piccerelle, P. & Andrieu, V. Recent advances in ocular drug delivery. *Drug Dev. Ind. Pharm.* **39**, 1599–1617 (2013).

37. Wang, W. et al. Engineering micro oxygen factories to slow tumour progression via hyperoxic microenvironments. *Nat. Commun.* **13**, 4495 (2022).

38. Zhu, Y. et al. DNMT1-mediated PPARα methylation aggravates damage of retinal tissues in diabetic retinopathy mice. *Biol. Res.* **54**, 25 (2021).

39. Gomes, S. I. L., Neves, A. B., Scott-Fordsmand, J. J. & Amorim, M. J. B. Reactive oxygen species detection using fluorescence in Enchytraeus crypticus-method implementation through Ag NM300K case study. *Toxics* **9**, 232 (2021).

40. Kim, J., Park, H., Saravanakumar, G. & Kim, W. J. Polymer/aptamer-integrated gold nanoconstruct suppresses the inflammatory process by scavenging ROS and capturing pro-inflammatory cytokine TNF-α. *ACS Appl. Mater. Interfaces* **13**, 9390–9401 (2021).

41. Guo, J. et al. Cyclodextrin-derived intrinsically bioactive nanoparticles for treatment of acute and chronic inflammatory diseases. *Adv. Mater.* **31**, e1904607 (2019).

42. Yan, X. et al. Silver nanoclusters show advantages in macrophage tracing in vivo and modulation of anti-tumor immuno-microenvironment. *J. Control Release* **348**, 470–482 (2022).

43. Dinarello, C. A. Anti-inflammatory agents: present and future. *Cell.* **140**, 935–950 (2010).

44. Mahboubi Rabbani, S. M. I. & Zarghi, A. Selective COX-2 inhibitors as anticancer agents: a patent review (2014-2018). *Expert Opin. Ther. Pat.* **29**, 407–427 (2019).

45. Liang, W. C. et al. Signaling mechanisms of growth hormone-releasing hormone receptor in LPS-induced acute ocular inflammation. *Proc. Natl. Acad. Sci. USA* **117**, 6067–6074 (2020).

46. Wang, S. H. et al. Palladium nanoplates scotch breast cancer lung metastasis by constraining epithelial-mesenchymal transition. *Natl. Sci. Rev.* **8**, nwaa226 (2021).

47. Huang, Y. et al. Quantitative structure-activity relationship models for predicting inflammatory potential of metal oxide nanoparticles. *Environ. Health Perspect.* **128**, 67010 (2020).

48. Leal, S. M. Jr et al. Distinct roles for Dectin-1 and TLR4 in the pathogenesis of Aspergillus fumigatus keratitis. *PLoS Pathog.* **6**, e1000976 (2010).

49. Wu, T. G., Wilhelmus, K. R. & Mitchell, B. M. Experimental keratomycosis in a mouse model. *Invest. Ophthalmol. Vis. Sci.* **44**, 210–216 (2003).

50. Singh, P. K. et al. 1, 3β-Glucan anchored, paclitaxel loaded chitosan nanocarrier endows enhanced hemocompatibility with efficient anti-glioblastoma stem cells therapy. *Carbohydr. Polym.* **180**, 365–375 (2018).

51. Garcia-Fuentes, M. & Alonso, M. J. Chitosan-based drug nanocarriers: where do we stand? *J. Control Release* **161**, 496–504 (2012).

52. Caprifico, A. E., Polycarpou, E., Foot, P. J. S. & Calabrese, G. Fluorescein isothiocyanate chitosan nanoparticles in oral drug delivery studies. *Trends Pharmacol. Sci.* **41**, 686–689 (2020).

53. Younes, I. & Rinaudo, M. Chitin and chitosan preparation from marine sources. Structure, properties and applications. *Mar. Drugs* **13**, 1133–1174 (2015).

54. Shariatinia, Z. Carboxymethyl chitosan: properties and biomedical applications. *Int. J. Biol. Macromol.* **120**, 1406–1419 (2018).

55. Lan, W., He, L. & Liu, Y. Preparation and properties of sodium carboxymethyl cellulose/sodium alginate/chitosan composite film. *Coatings.* **8**, 291 (2018).

56. Patrulea, V., Ostafe, V., Borchard, G. & Jordan, O. Chitosan as a starting material for wound healing applications. *Eur. J. Pharm. Biopharm.* **97**, 417–426 (2015).

57. Sultana, T. et al. Multi-functional nanocellulose-chitosan dressing loaded with antibacterial lawsone for rapid hemostasis and cutaneous wound healing. *Carbohydr. Polym.* **272**, 118482 (2021).

58. Chang, S. H., Lin, H. T., Wu, G. J. & Tsai, G. J. pH Effects on solubility, zeta potential, and correlation between antibacterial activity and molecular weight of chitosan. *Carbohydr. Polym.* **134**, 74–81 (2015).

59. Wang, F. et al. Hybrid natural hydrogels integrated with voriconazole-loaded microspheres for ocular antifungal applications. *J. Mater. Chem. B* **9**, 3377–3388 (2021).

60. Zhang, X., Wei, D., Xu, Y. & Zhu, Q. Hyaluronic acid in ocular drug delivery. *Carbohydr. Polym.* **264**, 118006 (2021).

61. Jian, H. J. et al. Super-cationic carbon quantum dots synthesized from spermidine as an eye drop formulation for topical treatment of bacterial keratitis. *ACS Nano* **11**, 6703–6716 (2017).

62. Srinivasarao, D. A., Lohiya, G. & Katti, D. S. Fundamentals, challenges, and nanomedicine-based solutions for ocular diseases. *Wiley Interdiscip. Rev. Nanomed. Nanobiotechnol.* **11**, e1548 (2019).

63. Vaneev, A. et al. Nanotechnology for topical drug delivery to the anterior segment of the eye. *Int. J. Mol. Sci.* **22**, 12368 (2021).

64. El-Sawy, H. S., Al-Abd, A. M., Ahmed, T. A., El-Say, K. M. & Torchilin, V. P. Stimuli-responsive nano-architecture drug-delivery systems to solid tumor micromilieu: past, present, and future perspectives. *ACS Nano* **12**, 10636–10664 (2018).

65. Li, X. et al. Ischemic microenvironment-responsive therapeutics for cardiovascular diseases. *Adv. Mater.* **33**, e2105348 (2021).

66. Cheng, R., Meng, F., Deng, C., Klok, H. A. & Zhong, Z. Dual and multi-stimuli responsive polymeric nanoparticles for programmed site-specific drug delivery. *Biomaterials* **34**, 3647–3657 (2013).

67. Ma, G. et al. H_2O_2-responsive NIR-II AIE nanobomb for carbon monoxide boosting low-temperature photothermal therapy. *Angew. Chem. Int. Ed. Engl.* **61**, e202207213 (2022).

68. Ma, N. et al. Selenium-containing block copolymers and their oxidation-responsive aggregates. *Polym. Chem.* **1**, 1609–1614 (2010).

69. Li, C. et al. The role of LOX-1 in innate immunity to aspergillus fumigatus in corneal epithelial cells. *Invest Ophthalmol. Vis. Sci.* **56**, 3593–3603 (2015).

70. Wiederhold, N. P., Locke, J. B., Daruwala, P. & Bartizal, K. Rezafungin (CD101) demonstrates potent in vitro activity against Aspergillus, including azole-resistant Aspergillus fumigatus isolates and cryptic species. *J. Antimicrob. Chemother.* **73**, 3063–3067 (2018).